**Astronomy
&
Astrophysics**

The Fornax 3D project: Non-linear colour–metallicity relation of globular clusters[*]

K. Fahrion[1], M. Lyubenova[1], M. Hilker[1], G. van de Ven[2], J. Falcón-Barroso[3,4], R. Leaman[5], I. Martín-Navarro[6,4,7,5], A. Bittner[1], L. Coccato[1], E. M. Corsini[8,9], D. A. Gadotti[1], E. Iodice[1,10], R. M. McDermid[11], F. Pinna[5], M. Sarzi[12,13], S. Viaene[14], P. T. de Zeeuw[15,16], and L. Zhu[17]

[1] European Southern Observatory, Karl-Schwarzschild-Straße 2, 85748 Garching bei München, Germany
e-mail: kfahrion@eso.org
[2] Department of Astrophysics, University of Vienna, Türkenschanzstrasse 17, 1180 Wien, Austria
[3] Instituto de Astrofísica de Canarias, Calle Via Láctea s/n, 38200 La Laguna, Tenerife, Spain
[4] Depto. Astrofísica, Universidad de La Laguna, Calle Astrofísico Francisco Sánchez s/n, 38206 La Laguna, Tenerife, Spain
[5] Max-Planck-Institut für Astronomie, Königstuhl 17, 69117 Heidelberg, Germany
[6] Instituto de Astrofísica de Canarias, 38200 La Laguna, Tenerife, Spain
[7] University of California Santa Cruz, 1156 High Street, Santa Cruz, CA 95064, USA
[8] Dipartimento di Fisica e Astronomia "G. Galilei", Università di Padova, Vicolo dell'Osservatorio 3, 35122 Padova, Italy
[9] INAF–Osservatorio Astronomico di Padova, Vicolo dell'Osservatorio 5, 35122 Padova, Italy
[10] INAF-Astronomical Observatory of Capodimonte, Via Moiariello 16, 80131 Napoli, Italy
[11] Department of Physics and Astronomy, Macquarie University, North Ryde, NSW 2109, Australia
[12] Armagh Observatory and Planetarium, College Hill, Armagh BT61 9DG, UK
[13] Centre for Astrophysics Research, University of Hertfordshire, College Lane, Hatfield AL10 9AB, UK
[14] Sterrenkundig Observatorium, Universiteit Gent, Krijgslaan 281, 9000 Gent, Belgium
[15] Sterrewacht Leiden, Leiden University, Postbus 9513, 2300 RA Leiden, The Netherlands
[16] Max-Planck-Institut für Extraterrestrische Physik, Gießenbachstraße 1, 85748 Garching bei München, Germany
[17] Shanghai Astronomical Observatory, Chinese Academy of Sciences, 80 Nandan Road, Shanghai 200030, PR China

ABSTRACT

Globular cluster (GC) systems of massive galaxies often show a bimodal colour distribution. This has been interpreted as a metallicity bimodality, created by a two-stage galaxy formation where the red, metal-rich GCs were formed in the parent halo and the blue metal-poor GCs were accreted. This interpretation, however, crucially depends on the assumption that GCs are exclusively old stellar systems with a linear colour–metallicity relation (CZR). The shape of the CZR and range of GC ages are currently under debate because their study requires high quality spectra to derive reliable stellar population properties. We determined metallicities with full spectral fitting from a sample of 187 GCs with a high spectral signal-to-noise ratio in 23 galaxies of the Fornax cluster that were observed as part of the Fornax 3D project. The derived CZR from this sample is non-linear and can be described by a piecewise linear function with a break point at $(g - z) \sim 1.1$ mag. The less massive galaxies in our sample ($M_* < 10^{10} \, M_\odot$) appear to have slightly younger GCs, but the shape of the CZR is insensitive to the GC ages. Although the least massive galaxies lack red, metal-rich GCs, a non-linear CZR is found irrespective of the galaxy mass, even in the most massive galaxies ($M_* \geq 10^{11} \, M_\odot$). Our CZR predicts narrow unimodal GC metallicity distributions for low mass and broad unimodal distributions for very massive galaxies, dominated by a metal-poor and metal-rich peak, respectively, and bimodal distributions for galaxies with intermediate masses ($10^{10} \leq M_* < 10^{11} \, M_\odot$) as a consequence of the relative fraction of red and blue GCs. The diverse metallicity distributions challenge the simple differentiation of GC populations solely based on their colour.

Key words. galaxies: kinematics and dynamics – galaxies: star clusters: general – galaxies: clusters: individual: Fornax – galaxies: evolution

1. Introduction

Cosmological simulations provide a framework of galaxy formation and evolution via the hierarchical mergers of smaller galaxies, but the assembly of individual galaxies is challenging to constrain observationally. Globular clusters (GCs) are traditionally used to study galaxy assembly due to their ubiquitous occurrence in all massive galaxies ($M_* > 10^9 \, M_\odot$, see Brodie & Strader 2006). Their potential as tracers of galaxy evolution is based on their old ages ($\gtrsim 10$ Gyr, Puzia et al. 2005; Strader et al. 2005), which sets

their formation at a redshift of $z \gtrsim 2$, coinciding with the peak of cosmic star formation (Madau & Dickinson 2014; El-Badry et al. 2019; Reina-Campos et al. 2019). The survival of GCs until today allows us to view them as fossil records that have the chemo-dynamical properties of their origin encapsulated in their stellar population properties and orbital parameters which change only slowly over time (e.g. Brodie & Strader 2006; Beasley et al. 2008; Harris et al. 2016).

In context of galaxy assembly, the metallicity distribution function (MDF) of GCs is of particular importance. If GCs trace the metallicity of their birthplace, the diverse merger histories of major galaxies as predicted from cosmological simulations (e.g.

Kruijssen et al. 2019) translate into diverse shapes of the MDF and consequently, the shape of the MDF can put constraints on the merger history.

In many galaxies, the MDF was found to have a bimodal shape with a metal-poor ([Fe/H] ~ -1.5 dex) and a metal-rich component ([Fe/H] ~ -0.5 dex), for example in the Milky Way (MW, e.g. Harris & Canterna 1979; Zinn 1985), Centaurus A (NGC 5128, Beasley et al. 2008), and the Sombrero galaxy (M 104, Alves-Brito et al. 2011). The bimodality of the MDF is often interpreted as direct result of two-stage formation of massive galaxies (e.g. Zepf & Ashman 1993; Beasley et al. 2002; Brodie & Strader 2006; Harris 2010; Forbes et al. 2011; Cantiello et al. 2014; Kartha et al. 2016): the metal-rich GCs are thought to have formed primarily in situ in the parent halo, whereas the metal-poor GCs formed in less massive galaxies and were accreted during the assembly of the host (e.g. Côté et al. 1998, 2000; Hilker et al. 1999; Katz & Ricotti 2014). However, in some galaxies such as M 31, the bimodality of the GC MDF is debated (e.g. Barmby et al. 2000; Galleti et al. 2009), with recent studies indicating even a trimodal distribution (Caldwell & Romanowsky 2016). Broad multimodal MDFs were suggested in a photometric study of brightest cluster galaxies, the most massive early-type galaxies (ETGs, Harris et al. 2014, 2016, 2017), based on unimodal colour distributions, making the shape of the GC MDF a heavily discussed topic nowadays.

Because a detailed study of extragalactic GC MDFs requires time-expensive spectroscopy of individual GCs, often optical photometric studies of GC systems are used to infer the MDF from a colour distribution. These studies have shown that most massive galaxies have bimodal GC colour distributions (e.g. Kundu & Whitmore 2001; Larsen et al. 2001; Peng et al. 2006), and because GCs are usually old stellar systems (e.g. Strader et al. 2005), this colour bimodality is usually translated into a bimodal MDF. However, this convertion crucially depends on the shape of colour–metallicity relation (CZR, e.g. whether it is linear or not)[1]. Both Richtler (2006) and Yoon et al. (2006) suggested that a strongly non-linear CZR can produce bimodal colour distributions from broad unimodal metallicity distributions, challenging the view of a simple two-phase galaxy formation.

Also the choice of colour can affect the inferred colour distributions. Bimodal distributions are more commonly seen when using optical colours, while optical-near-infrared colours can show unimodal colour distributions for the same GC system (e.g. Blakeslee et al. 2012; Chies-Santos et al. 2012; Cho et al. 2016). These colour-colour non-linearities suggest a underlying non-linearity of the CZR in some colours, with the optical-near-infrared colours being least sensitive (Cantiello & Blakeslee 2007). However, the S0 galaxy NGC 3115 was found to show both non-linearities in colour-colour space as well as a bimodal metallicity distribution (Cantiello et al. 2014).

Due to the lack of large homogeneous samples of spectroscopic GC metallicities, there is no consensus on the shape of the CZR. Using the few spectroscopic GC metallicities available at that time, Peng et al. (2006) presented a piecewise linear CZR with a breakpoint at $(g − z) \sim 1.0$ mag. A similar description was found by Usher et al. (2012), however, with a breakpoint at bluer colours. Their result was based on a diverse sample of GC metallicities from five different massive galaxies, brought to the photometry scheme of the SAGES Legacy Unifying Globulars and Galaxies Survey (SLUGGS; Brodie et al. 2014). While these two studies combined GC metallicities from different galaxies, Sinnott et al. (2010) and Harris et al. (2017) proposed a CZR described by a quadratic function based on literature metallicities of Centaurus A. Recently, Villaume et al. (2019) presented a linear CZR based on metallicities of 177 GCs of M 87, the central galaxy of the Virgo cluster.

The different results on the shape of the CZR might be connected to different measurement techniques. But, it could also indicate that the CZR is not universal and possibly depends on the host galaxy or the environment. For example, Villaume et al. (2019) found a lack of metal-poor GCs in M 87 compared to other systems such as the MW. Usher et al. (2015) found indications for a CZR that varies from galaxy to galaxy and suggested this might be caused by different GC age distributions because the CZR strongly depends on the assumption that GCs are old stellar systems. Although many spectroscopic studies of extragalactic GCs have found generally old ages of $\gtrsim 12$ Gyr (e.g. Cohen et al. 1998; Forbes et al. 2001; Puzia et al. 2005; Norris et al. 2008), there are also examples of younger GCs in a few galaxies (e.g. Chandar et al. 2006; Sharina et al. 2006; Hempel et al. 2007; Martocchia et al. 2018; Sesto et al. 2018; Usher et al. 2019). These might cause deviations in the CZR due to the age-metallicity degeneracy (Worthey 1994).

In this paper, we present a non-linear CZR that was obtained using a sample of 187 GCs of 23 galaxies that were observed as part of the Fornax 3D project (F3D, Sarzi et al. 2018), a magnitude-limited survey with the Multi Unit Spectroscopic Explorer (MUSE) on the Very Large Telescope of bright galaxies within the virial radius of the Fornax cluster. The GCs we use in this work are a sub-sample of the GC catalogue presented in Fahrion et al. (2020, hereafter Paper I), in which we tested the ability of GCs as tracers of kinematics and stellar population properties. Because F3D covers both ETGs and late-type galaxies (LTGs) with masses ranging between 10^8 and 10^{11} $M_\odot$, we can explore a sample of GCs over a variety of galaxy masses. In Paper I, we found that especially the red GCs closely trace the metallicity of the host galaxy, even in the inner parts of galaxies, while the blue GCs are significantly more metal-poor at all radii. In the current paper, we extend the analysis of GC metallicities to derive a CZR from a well sampled range of GC colours without the need to combine metallicity measurements from different studies. While most previous works have focused on rather massive galaxies with $M_* > 10^{10}$ $M_\odot$, we can explore the effect of the host galaxy on the CZR because of the broad mass range of galaxies in F3D.

We describe the GC sample in the next section and the methods for the stellar population measurements are briefly described in Sect. 3. Section 4 presents our results for the CZR and describes tests to validate the measured metallicities. We also present estimates of GC ages and the mass-metallicity relation (MZR) of our sample. In Sect. 5, we discuss our findings in relation to the literature and describe possible implications for galaxy evolution. We summarise and present our results and conclusions in Sect. 6.

2. Globular cluster sample

We described the extraction and basic analysis of a sample of 722 spectroscopically confirmed GCs in 32 galaxies of the Fornax cluster in Paper I. These galaxies were observed as part of F3D and details on the MUSE observations can be found in Sarzi et al. (2018) and Iodice et al. (2019). The spectra of these GCs were directly extracted from the MUSE cubes and

---

[1] We chose CZR as abbreviation to prevent possible confusion with the term "colour–magnitude relation".

Table 1. Overview of the GC sample used in this work.

Galaxy	Altern. name	Morphology	R_{proj} (Mpc)	$\log(M_*/M_\odot)$	$N_{S/N \geq 8,\, r>15''}$	$\langle R_{\mathrm{GCs}} \rangle$ (R_{eff})
(1)	(2)	(3)	(4)	(5)	(6)	(7)
FCC083	NGC 1351	E5	0.58	10.5	15	0.70
FCC090	PGC 13058	E4	0.57	8.9	1	1.11
FCC113	ESO 358−015	Scd	0.43	8.3	1	0.75
FCC143	NGC 1373	E3	0.26	9.4	3	1.91
FCC147	NGC 1374	E0	0.22	10.4	18	1.20
FCC148	NGC 1375	S0	0.22	9.8	2	2.10
FCC153	IC 1963	S0	0.40	9.9	1	1.26
FCC161	NGC 1379	E0	0.17	10.4	27	0.97
FCC167	NGC 1380	S0	0.21	11.0	16	0.68
FCC170	NGC 1381	S0	0.14	10.4	9	2.00
FCC176	NGC 1369	SB	0.30	9.8	1	0.41
FCC177	NGC 1380A	S0	0.27	9.9	6	0.68
FCC182	–	SB0	0.11	9.2	2	1.74
FCC184	NGC 1387	SB0	0.11	10.7	18	1.25
FCC190	NGC 1380B	SB0	0.13	9.7	9	1.22
FCC193	NGC 1389	SB0	0.13	10.5	1	0.72
FCC213	NGC 1399	E1	0	11.4	25	0.12
FCC219	NGC 1404	E2	0.06	11.1	3	0.22
FCC249	NGC 1419	E0	0.71	9.7	3	1.72
FCC255	ESO 358-G50	S0	0.60	9.7	3	1.38
FCC276	NGC 1427	E4	0.27	10.3	19	0.77
FCC290	NGC 1436	Sc	0.38	9.8	1	0.34
FCC308	NGC 1437B	Sd	0.60	8.6	3	1.40

Notes. (1) Galaxy name from Ferguson (1989) and (2) alternative name. (3) Galaxy morphology. (4) Projected distance from FCC 213. (5) Stellar mass from Iodice et al. (2019) and Liu et al. (2019). (6) Number of GCs with $S/N > 8$ and galactocentric distance $>15''$. (7) Mean galactocentric distance of the F3D GCs. This refers to all GCs (see Paper I).

for each GC, a spectrum of the local galaxy background was subtracted. Because F3D targets the central regions of galaxies (up to $\sim 3\,R_{\mathrm{eff}}$), this cleaning process is necessary to remove the galaxy contribution that otherwise heavily contaminates the GC spectrum. Each GC spectrum was then classified by its spectral signal-to-noise ratio (S/N). Compared to the ACSFCS catalogue (Jordán et al. 2015), we reached a completeness of ~50% at an absolute g-band magnitude of $M_g \sim -8$ mag.

In the first paper, we derived line-of-sight (LOS) velocities from all GC spectra with $S/N \geq 3\,\text{Å}^{-1}$, and metallicities for the GCs with $S/N \geq 8\,\text{Å}^{-1}$. For the present work, we only include GCs with a galactocentric distance $r_{\mathrm{gal}} \geq 15''$ because testing has shown that the spectra of GCs with small galactocentric distances can still be contaminated by residual galaxy light that strongly varies in the central regions. These GCs can be biased to higher metallicities because the host galaxy tends to be more metal-rich than the GCs, especially in the centre. From the initial sample of 722 GCs, this cut in S/N and galactocentric distance leaves a sub-sample of 187 GCs in 23 galaxies. Table 1 gives an overview of this sub-sample and lists the number of available GC metallicities per galaxy. The majority of GCs were found in ETG hosts.

3. Extraction of stellar population properties

We describe how the stellar population properties were derived from the GC spectra in the following section. Besides the default approach of measuring metallicities discussed in the main text, we tested other approaches to derive metallicities as described in Appendix A.

3.1. Full spectral fitting with pPXF

We used the penalised Pixel-fitting (PPXF) method (Cappellari & Emsellem 2004; Cappellari 2017) to obtain metallicities of GCs with $S/N \geq 8\,\text{Å}^{-1}$. PPXF uses a penalised maximum likelihood approach to fit spectra with a combination of user-provided template spectra and allows to determine best-fit age and metallicity distributions from a library of single stellar population (SSP) models (e.g. Pinna et al. 2019; Boecker et al. 2019; Fahrion et al. 2019a,b). We used the E-MILES SSP models (Vazdekis et al. 2016), that have broad wavelength coverage from 1680 to 50 000 Å. The model spectra are sampled at 1.25 Å at a spectral resolution of ~2.5 Å (Falcón-Barroso et al. 2011) in the wavelength range of interest, approximately corresponding to the mean instrumental resolution of MUSE. We used additive polynomials of degree 12 for the extraction of LOS velocities and multiplicative polynomials of degree 8 for the stellar population measurements.

Throughout this work, we used SSP models based on BaSTI isochrones (Pietrinferni et al. 2004, 2006) and a MW-like double power law (bimodal) initial mass function with a high mass slope of 1.30 (Vazdekis et al. 1996). The models provide a grid of SSPs with ages between 300 Myr and 14 Gyr and metallicities between $[M/H] = -2.27$ and $+0.40$ dex. Because PPXF returns the weights of the best-fitting combination of SSP models, the stellar populations of a GC can be described by the weighted mean age and metallicity. As described in Paper I, we fitted each GC spectrum in Monte-Carlo-approach to derive reliable random uncertainties by perturbing the spectrum 100 times based on the residuals from the first fit. These fits were done with a

restricted library that only contains SSP templates with stellar ages ≥ 8 Gyr. This limits the effect of a possible age-metallicity degeneracy and speeds up the fitting process. To explore the influence of this choice, we also fitted a sub-sample of 135 GCs with $S/N > 10$ Å without any constraint on the age. The results of the GC ages are described in Sect. 4.2.

To determine reliable metallicities from the GC spectra, we used the E-MILES SSP models because their broad wavelength coverage helps to reduce uncertainties. For E-MILES, only so-called baseFe models are available that are based on empirical stellar spectra and thus inherit the abundance pattern of the MW. They are α-enhanced at low metallicities and follow [Fe/H] = [M/H] at high metallicities. As this abundance pattern might not represent the GCs in the Fornax cluster, we determined the [α/Fe] abundances of a sub-sample of GCs with the highest S/N (>20 Å^{-1}) using α-variable MILES models that are based on the standard MILES models which only offer two different [α/Fe] values of 0 (scaled solar) and 0.4 dex (α-enhanced). The α-variable MILES models were created using a linear interpolation between these to create a regular grid from [α/Fe] = 0 to [α/Fe] = 0.4 dex with a spacing of 0.1 dex. Because these α-variable MILES models introduce another free parameter that can be fitted, only GCs with the highest S/Ns give reasonable results. The measured abundance pattern (see Sect. 4.3) of the high S/N GCs further supports the use of the E-MILES models as our default approach.

To summarise, our default approach was to fit the GCs with $S/N \geq 8$ Å^{-1} with the E-MILES SSP models and an age constraint of ≥8 Gyr. We tested the effects of GC age by fitting GCs with $S/N > 10$ Å^{-1} without age constraint and determined [α/Fe] abundances only for the brightest GCs with $S/N > 20$ Å^{-1}. The latter two approaches are to validate the results from our default approach. In Appendix A, we further explore the choice of SSP models and also test metallicities from line-strength indices.

3.2. Globular cluster colours

We used $(g - z)$ colours, mostly from the photometric GC catalogues of Jordán et al. (2015) that were obtained as part of the ACS Fornax Cluster Survey (ACSFCS; Jordán et al. 2007). These catalogues report the magnitudes of the GC candidates in the ACS $F475W$ (~g band) and $F850LP$ (~z band).

Not all galaxies in our sample were covered by the ACSFCS and consequently, 45 GCs in our sample have no ACS colours available. For those, we determined synthetic $(g - z)$ colours from the MUSE spectra using the $F475W$ and $F850LP$ transmission curves. While the $F475W$ band is covered completely with MUSE, the $F850LP$ bandpass extends outside the MUSE coverage. In the colour regime covered by the 45 GCs without ACS photometry, the synthetic colours agree with the ACSFCS colours within a scatter of ~0.05 mag.

4. Results

In the following, we present the results from the stellar population analysis of the F3D GCs. We first discuss the colour–metallicity relation (CZR) and then address GC ages, α-abundances and the relation between mass and metallicity.

4.1. Colour metallicity relation

We plot the distribution of colours and metallicities of our F3D GCs in Fig. 1. This figure shows the relation between
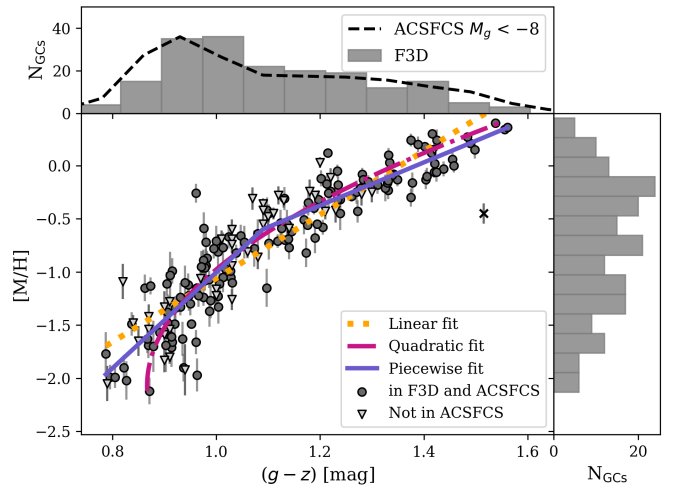
Fig. 1. Colour–metallicity distribution of F3D GCs. Spectroscopic GC metallicities from full spectral fitting versus $(g - z)$ colour. Filled circles and triangles refer to GCs with and without ACSFCS $(g - z)$ colours from Jordán et al. (2015), respectively. For the latter, we obtained the colour from the MUSE spectrum directly. The orange, pink and purple lines give the fit using the linear, quadratic or piecewise function (Eqs. (1)–(3)). The corresponding residuals are found in Fig. 2. As described in the text, we excluded an outlier from the fit marked by a cross. Separate distributions of colour and metallicities are shown on the top and the right-hand side. *Top panel*: we included the histogram from the full ACSFCS GC sample after applying a magnitude cut corresponding to our sample.

the $(g - z)$ colours and spectroscopic total metallicity [M/H] as derived based on the E-MILES SSP models for the GCs with $S/N \geq 8$ Å^{-1}. Although most of the GCs were covered by the ACSFCS and have HST colours, the CZR is better constrained when also including GCs with synthetic MUSE colours. There is one outlier with a ACSFCS colour of $(g - z) \sim 1.5$ mag and a metallicity of ~−0.5 dex that lies significantly below the relation. This is a GC found in the halo pointing of FCC 167 with a synthetic MUSE colour of $(g - z) \sim 1.2$ mag that would place it among the bulk of GCs. Usually, the synthetic colours agree within ±0.05 mag with the ACSFCS colours, making this GC an outlier and because the origin of the large colour difference is unknown, we excluded this GC from the fit. Another visible outlier that lies above the relation at $(g-z) \sim 1.0$ is a GC found in the central pointing in FCC 276 with a small galactocentric distance of 16″. Since FCC 276 is quite massive ($\log(M_*/M_\odot) \sim 10.3$), it is possible that the spectrum of this GC is still contaminated by the bright galaxy background which could bias the measured metallicity to higher values.

The top panel of Fig. 1 compares the colour histogram of the F3D GCs to the full sample of ACSFCS GCs (Jordán et al. 2015), normalised to match the peak in our GC distribution. We only have metallicity estimates from GCs with spectral $S/N \geq 8$ Å^{-1}. As we showed in Paper I, these are GCs with $M_g \lesssim -8$ mag. Therefore, we apply the same brightness cut to the full ACSFCS sample. Our GC sample is representative of the bright GC population of the ACSFCS cluster survey, and the full colour range from 0.8 to 1.6 mag is well sampled. There is a large number of GCs with $(g-z) \sim 1$ mag, but our sample shows a deficit of GCs at very blue colours <0.8 mag, possibly because those are expected to be very metal-poor and consequently the absence of strong absorption lines in the spectrum leads to lower S/N.
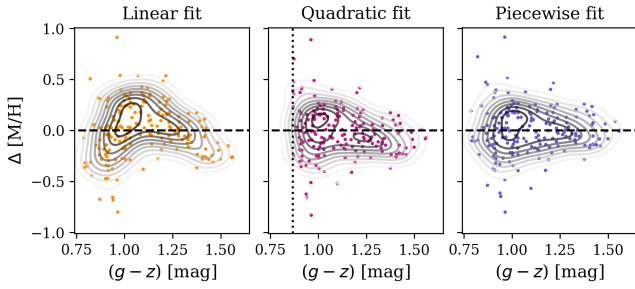
Fig. 2. Residuals when fitting the colour–metallicity distribution shown in Fig. 1 with a linear (*left*), a quadratic (*middle*) and piecewise linear function (*right*), respectively. Coloured points show the observed scatter and the contours give a kernel density estimation using an arbitrary Gaussian kernel for visualisation of the residual shape. The dotted vertical line in the *middle panel* shows where the quadratic model diverges.

Our GC sample contains the most massive GCs of the total population and in order to apply our relation to the full GC distribution (see Sect. 5.3), we have to assume that the less massive GCs follow the same relation. In Sect. 4.4, we report on the mass-metallicity relation (MZR) of GCs and show that the metallicity does not depend strongly on the GC stellar mass. The less massive GCs missing from our sample are expected to be even more metal-poor and thus it is unlikely that they would change the shape of the CZR. In addition, the colour span around $(g - z) \sim 1$ mag, where we observe the break in the relation, is already well sampled.

To quantitatively describe the CZR, we fitted the distribution with different functions using a least-square algorithm. The best-fitting functions are shown as coloured lines in Fig. 1 and we show the respective residuals in Fig. 2. Using a simple linear function gives a relation of the following form:

$$[M/H] = (-4.05 \pm 0.11) + (2.99 \pm 0.10)\,(g - z). \tag{1}$$

As Fig. 2 shows, the residual of this linear fit shows a bent shape. At very blue and red colours, the metallicities are overestimated and are underestimated at intermediate colours.

In order to improve the quantitative description of the CZR, we used a quadratic relation to fit the CZR (see also Sinnott et al. 2010; Harris et al. 2017):

$$(g - z) = a\,[M/H]^2 + b\,[M/H] + c. \tag{2}$$

The least-square fit returned best-fitting paramters of $a = 1.34 \pm 0.01$, $b = 0.46 \pm 0.02$, $c = 0.11 \pm 0.01$. This best-fitting relation is shown by the pink line in Fig. 1. The residual shows a more symmetric shape than when using the linear fit.

In addition, we used a piecewise linear function, similar to that of Peng et al. (2006):

$$[M/H] = b_1 + m_1(g - z) \quad \text{for } (g - z) < x_0$$
$$= b_2 + m_2(g - z) \quad \text{for } (g - z) \geq x_0, \tag{3}$$

with best-fitting parameters of $m_1 = 4.51 \pm 0.32$, $b_1 = -5.51 \pm 0.36$, $m_2 = 2.03 \pm 0.20$, $b_2 = -2.81 \pm 0.36$, and $x_0 = 1.09 \pm 0.03$ (purple line in Fig. 1). The residual is more symmetrical around the zero line (Fig. 2).

Comparing the residuals of the fitted relations shows that the linear fit is insufficient to capture the shape of the CZR accurately. The quadratic and piecewise relations return similar residuals, however, the quadratic relation shows an asymptotic behaviour for colours $(g - z) < 0.86$ mag, although our sample reaches bluer colours. To compare the models quantitatively, we
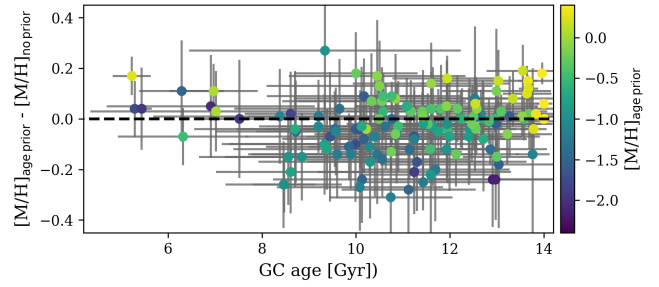

Fig. 3. Difference of GC metallicities from PPXF when using or not an age prior (≥ 8 Gyr) in relation to the best-fitting age. The symbols are colour-coded by the best-fitting metallicity. The dashed line shows the zero difference.

derived the Bayesian information criterion (BIC) for each model. The piecewise linear relation has the lowest BIC and is preferred over the linear model by $\Delta BIC = 32$ and over the quadratic model by $\Delta BIC = 35$. While the residual scatter is comparable for the piecewise and the quadratic model, the asymptotic behaviour of the latter reduces the number of observables and thus increases the BIC. We conclude that the piecewise relation best represents the data.

4.2. Globular cluster ages

While our standard approach for fitting the GC spectra assumes an age ≥ 8 Gyr, we also fitted a sub-sample of 135 GCs with high S/N without any constraints on the age. Because of the larger SSP model grid, these fits take substantially longer, but allow us to study the effect of GC ages on the CZR due to a possible age-metallicity degeneracy. Therefore, in Fig. 3, we plot the GC metallicities from the default approach (with age prior) and without age constraint as a function of the best-fitting age. The metallicities from both methods agree within the uncertainties and there seems to be no trend with age. With very few exceptions, the GCs show best-fitting ages ≥ 8 Gyr, validating our choice of restricting the model grid for the PPXF fit.

Consequently, fitting without age constraint results in a similar non-linear CZR as is shown in Fig. A.1 in the appendix with best-fitting parameters presented in Table A.2. We can therefore conclude that the shape of the CZR cannot be explained by an underlying age-metallicity degeneracy.

The reddest, most metal-rich GCs in the sampe have very small age and metallicity uncertainties. For them, it is likely that the small uncertainties are an effect of the limited SSP grid. Otherwise, the GC ages have typical random uncertainties of >2 Gyr, reflecting the challenging age determination of old stellar populations (e.g. Usher et al. 2019, or appendix in Fahrion et al. 2019b). The wavelength coverage of MUSE is further lacking age sensitive spectral features such as higher Balmer lines.

The upper panel in Fig. 4 shows the age-metallicity distribution of the F3D GCs, colour-coded by the stellar mass of the host (Liu et al. 2019; Iodice et al. 2019). This figure suggests a shallow age-metallicity correlation of the GCs in which more metal-rich GCs are also older. This trend is mainly driven by the reddest, most metal-rich GCs that show very small age and metallicity uncertainties. As mentioned, it is likely that these GCs exceed the metallicities of the SSP models, or are strong α-enhanced, as was found for several GCs of massive ETGs (e.g. Puzia et al. 2005, 2006; Woodley et al. 2010a). The other GCs show a very mild correlation between age and metallicity that also coincides with a relation between host mass and GC age.
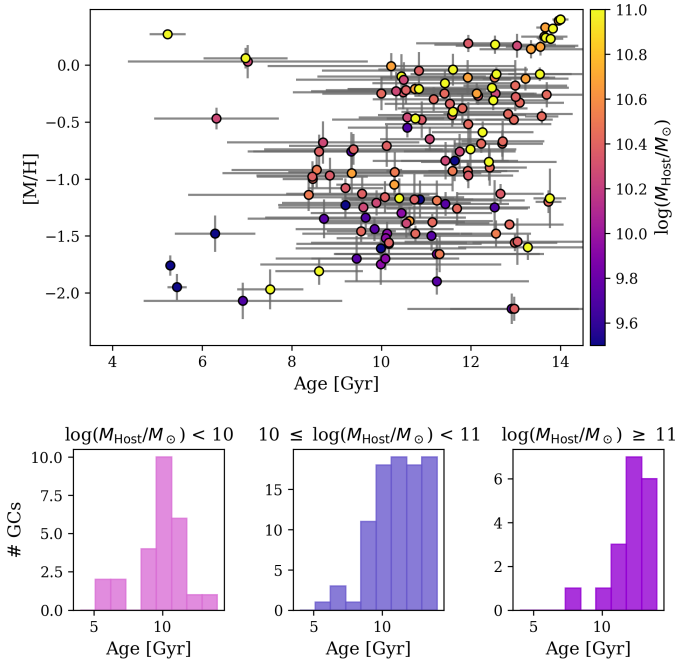
Fig. 4. *Top*: best-fitting ages and metallicities of GCs, inferred from full spectral fitting with the E-MILES templates and no age constraint. The colour coding refers to the stellar mass of the host galaxy (Iodice et al. 2019; Liu et al. 2019). *Bottom*: GC age distributions for host galaxies in three different mass bins.

To illustrate this, we binned the GC sample based on the stellar mass of the host galaxy into three mass bins and the bottom panel of Fig. 4 shows the GC age distribution in these mass bins. The GCs with the lowest host masses ($\log(M_{\mathrm{Host}}/M_\odot) < 10$) show a peak at 10 Gyr, whereas the intermediate and high mass bins show distributions that are dominated by very old ages. While the intermediate mass bin ($10 < \log(M_{\mathrm{Host}}/M_\odot) < 11$) shows some GCs with ages < 10 Gyr, these slightly younger GCs are apparently missing in the highest mass bin ($\log(M_{\mathrm{Host}}/M_\odot) > 11$). Although the number of GCs in each mass bin is quite low and the age uncertainties are large, we found indications that the lower mass hosts indeed have younger GC systems. Indications for such a trend were also found, for example, by Usher et al. (2019) when comparing three SLUGGS galaxies, possibly due to a top-down formation of GCs that form later in less massive galaxies. Moreover, such a behaviour is in agreement with a mass-dependent age-metallicity relation (see Leaman et al. 2013; Böcker et al. 2020 and references therein). Because low mass galaxies also tend to have more metal-poor GCs, the observed weak age-metallicity correlation might be driven by the host mass.

4.3. Abundance pattern of GCs

We obtained [α/Fe] values for the 31 brightest GCs in our sample that have $S/N > 20\,\text{Å}^{-1}$ using full spectral fitting with α-variable MILES models. We show the [α/Fe] values in relation to the iron metallicities of these GCs in the left panel of Fig. 5. This figure illustrates that these GCs show an negative correlation between metallicity and α-abundance with the metal-poor GCs being more α-enhanced.

The GCs therefore seem to follow a similar abundance pattern as the MW stars used to create the E-MILES SSPs. This is shown in the right panel of Fig. 5, where we plot the relationship between iron and total metallicity for the MILES stars

and the F3D GCs. Although the sample of GCs is limited, they seem to follow the same trend. This indicates that the E-MILES SSP models are indeed a reasonable choice to use with the GC spectra.

For this reason, we used the [M/H]−[Fe/H] relation of the MILES stars to establish a conversion between total and iron metallicities for the E-MILES GC metallicities. The purple line in Fig. 5 shows a least-square piecewise fit to the MILES stars (Eq. (3)) with parameters: $m_1 = 0.99 \pm 0.03$, $b_1 = -0.28 \pm 0.17$, $m_2 = 1.25 \pm 0.02$, $b_2 = -0.06 \pm 0.18$, and $x_0 = -0.83 \pm 0.11$.

4.4. Mass-metallicity relation

We determined the stellar masses of all GCs with ACSFCS colours using their measured metallicities and the photometric predictions from the E-MILES models that give the stellar mass-to-light ratio for a given model[2]. Assuming an average distance to the Fornax cluster of 20.9 Mpc (Blakeslee et al. 2009), we converted the g-band magnitudes from the ACSFCS (Jordán et al. 2015) to luminosities and then translated those to stellar masses. This results in the MZR shown in Fig. 6. We found GC masses between a few $10^5\,M_\odot$ and a few $10^7\,M_\odot$, representative of the more massive GC population. In this figure, the MZR of the GCs is compared to a MZR for GCs of M 87 (Zhang et al. 2018). They also reported the MZR for ultra compact dwarfs (UCDs) which is shallower than that of the GCs.

We fitted a log-linear function to describe the MZR:

$$[\mathrm{M/H}] = -20.58 + 3.08 \log(M_{*,\mathrm{GC}}/M_\odot). \qquad (4)$$

We found indications that the more massive galaxies have more massive GCs at the same metallicity. This could also explain the offset with respect to the relation from Zhang et al. (2018) because M 87 is significantly more massive than the galaxies included in our sample. However, the steepness of this relation shows that the metallicity of the GCs is not influenced strongly by the stellar mass of the GC, although there is a weak correlation. The less massive GCs tend to be more metal-poor and consequently, it is unlikely that including fainter GCs into the CZR would change the shape.

The MZR can also give insights into the origin of the so-called blue tilt, an observed optical colour–magnitude relation of blue GCs that describes that the brighter GCs of the blue GC population tend to be redder (e.g Harris et al. 2006; Spitler et al. 2006; Strader et al. 2006; Mieske et al. 2006). This has often been interpreted as an result of an underlying MZR of GCs, where the more massive GCs can retain more metals and thus have redder colours (e.g. Strader & Smith 2008; Bailin & Harris 2009), and also in combination with a non-linear CZR, a blue tilt can be observed (Blakeslee et al. 2010). Recently, Usher et al. (2018) used simulations to explore the origin of the blue tilt and suggested that its origin lies in the lack of massive metal-poor GCs because those would require special formation conditions with high gas densities in a metal-poor environment. The weak MZR we found is in accordance with this picture.

5. Discussion

We discuss our derived CZR with the literature as follows. We also explore the dependence of the CZR on the stellar mass of the host and discuss the implications of our findings.
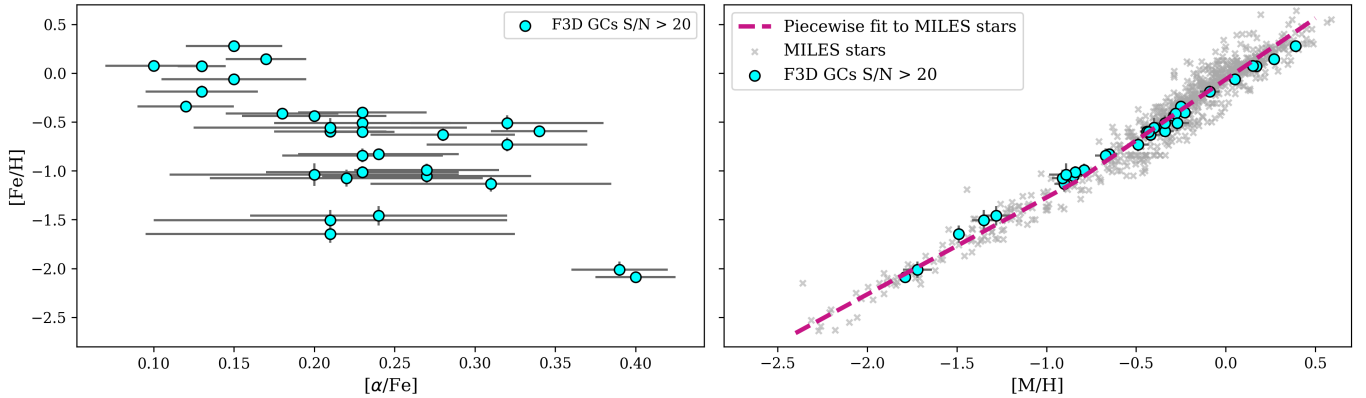
Fig. 5. Abundance pattern of F3D GCs. [Fe/H] in relation to [α/Fe] (*left*) and [M/H] (*right*). *Right panel*: the grey crosses show the distribution for the MILES stars that were used to construct the E-MILES models and the purple line is a least-square fit with a piecewise linear function (Eq. (3)) to the MILES stars. The cyan circles show the brightest F3D GCs in our sample.
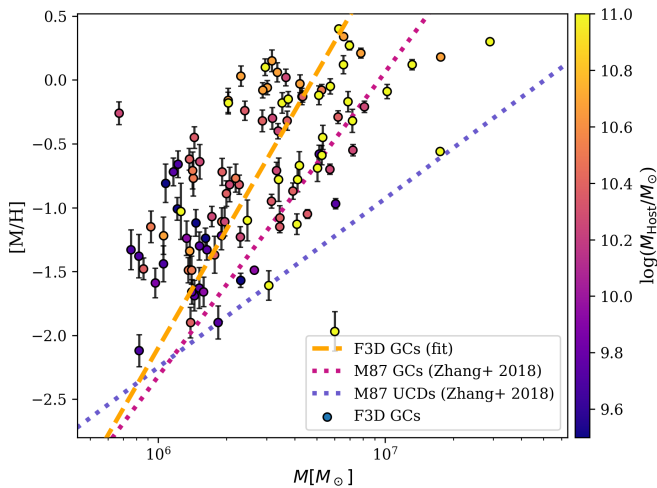

Fig. 6. MZR for the F3D GCs in comparison to the MZR for GCs and UCDs in M 87 (pink and purple dotted lines, respectively, Zhang et al. 2018). The least-square fit to our data is shown in orange. The F3D GCs are colour-coded by the stellar mass of their host.

5.1. Comparison to literature

Our CZR is compared to findings from the literature in Fig. 7, shown by lines of different colours. We differentiate between relations based on total and iron metallicities to avoid further conversions between them. For our sample, we used the conversion derived in Sect. 4.3 to convert them from [M/H] to [Fe/H]. The best-fit parameters of the CZR based on iron metallicities can be found in Table A.2.

Peng et al. (2006) studied the bimodality of GC colours in the Virgo cluster using HST/ACS photometry and $(g-z)$ colours. They derived a CZR from the few spectroscopic GC metallicity measurements of the MW, M 87 and M 49 that were available at that time (Harris 1996; Cohen et al. 1998, 2003). Their CZR is described by a piecewise linear relation with a break at $(g-z) \approx 1.05$ mag. As Fig. 7 shows, their relation is close to ours, especially for the blue GCs. At redder colours their relation is shallower. As Villaume et al. (2019) discussed, the break in the Peng et al. (2006) relation might be mainly caused by the MW GCs that are significantly more metal-poor than those of M 87.

Faifer et al. (2011) studied the GC systems of five massive ETGs with photometry in the g and i-bands of the

Gemini Multi-Object Spectrograph. Using literature metallicities (Pierce et al. 2006a,b; Norris et al. 2008), they found a linear CZR which is shown by the green line in Fig. 7. We converted their $(g' - i')$ colours to $(g - z)$ using the translation given in the appendix of Usher et al. (2012). Their relation predicts higher GC metallicities at all colours, although the slope is very similar to that of Usher et al. (2012), who used literature metallicities from Kuntschner et al. (2002), Brodie et al. (2005), Cenarro et al. (2007), Chomiuk et al. (2008), Caldwell et al. (2011) and SLUGGS $(g - i)$ photometry, to derive a piecewise CZR shown by the orange line in Fig. 7. This relation fits the red GCs of our sample quite well, but the break point is located at colour of $(g - z) \approx 0.84$ mag. The position of the break point is strongly driven by the metallicities of M 31 GCs (Caldwell et al. 2011) because the other galaxies in this collection show no GC metallicities < -1.2 dex. In the sample, M 31 is also the only LTG, while the others are massive ETGs.

Using metallicities from Woodley et al. (2010b) and *griz* photometry, Sinnott et al. (2010) presented a quadratic CZR for GCs of the giant elliptical Centaurus A. Harris et al. (2017) used the same metallicities, but combined the *griz* photometry of Sinnott et al. (2010) with *UBVRI* photometry available from Peng et al. (2004) to derive a very similar quadratic relation using $(g - I)$ colours. They also give conversion to $(g - z)$ colours (see also Choksi & Gnedin 2019). Their CZR is offset to our red GCs and shallower at blue colours.

Very recently, Villaume et al. (2019) presented a sample of 177 GCs of M 87 with spectroscopic metallicities and found a linear relation shown in Fig. 7. Their CZR follows the relation of Harris et al. (2017) at red colours and shows a deviation from our relation at the bluest GC colours. Villaume et al. (2019) discussed that their findings of more metal-rich blue GCs could indicate an environmental effect caused by the assembly history of M 87 itself.

The comparison to literature CZR highlights the diversity of relations that were found using different techniques and studies of different environments. In general, it appears that studies focusing on massive ETGs generally find linear relations due to a lack of metal-poor GCs. Non-linear relations are predominantly found when incorporating measurements of metal-poor GCs, for example, from the MW or M 31. This could indicate that massive ETGs indeed have a different CZR, whereas it is also possible that the lack of metal-poor GCs is due to selection effects and limited sample sizes because the most massive galaxies are dominated by more metal-rich GCs. Additionally, the radial extent of
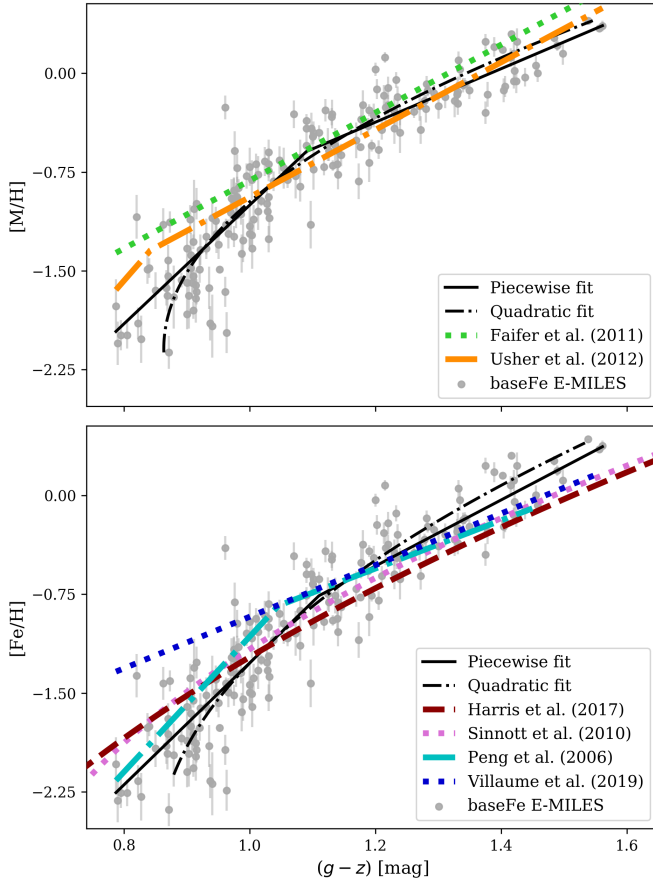
Fig. 7. Our CZR in comparison to literature results. We differentiate between relations based on total metallicities (*top*) and iron metallicities (*bottom*). The black curves give our fits (Table A.2). The green line in the top plot refers to the relation of Faifer et al. (2011) of five massive ETGs and the orange line shows the piecewise relation of Usher et al. (2012). Both relations were converted from $(g−i)$ colours to $(g−z)$ using the translations given in Usher et al. (2012). *Bottom panel*: quadratic relations of Sinnott et al. (2010) and Harris et al. (2017) (pink and red lines) obtained for GCs of Centaurus A and linear relation of Villaume et al. (2019) based on metallicities of GCs of M 87 (dark blue line). The bright blue line shows the piecewise relation from Peng et al. (2006) obtained from a diverse sample of literature metallicities.

the studied GCs can bias the selection as the blue GC population usually is more extended (e.g. Harris et al. 2016) and thus concentrating on the inner regions of massive galaxies can result in a lack of blue GCs. However, because our sample uses a large variety of galaxy masses, also the metal-poor end of the CZR is well sampled.

5.2. Dependence of the CZR on host mass

Usher et al. (2015) suggested that different galaxies can show variations in the CZR as a result of different assembly histories. In particular, the mass of the host galaxy might have an influence on the CZR, as was also suggested for M 87 (Villaume et al. 2019). With the F3D sample, we can test this to some extent as seen in Fig. 8. In this figure, we binned the total GC sample by the stellar mass of the host using three bins.

The lowest mass bin ($\log(M_*/M_\odot) < 10$) populates the blue, metal-poor end of the CZR. Fitting only these GCs results in a linear CZR with a steep slope similar to that we found at the blue end using the full sample. The linear fit also suggests a lower
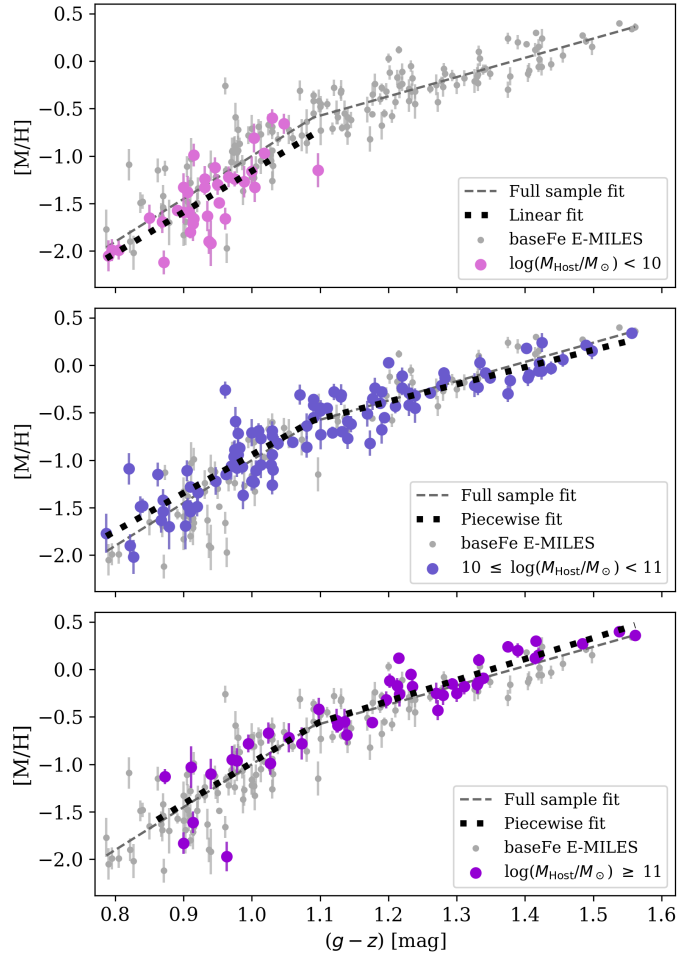

Fig. 8. CZR for GCs that are hosted by galaxies of different stellar masses. We binned the sample into three mass bins. *Top*: pink circles show GCs for galaxies with stellar masses $\log(M_{\mathrm{Host}}/M_\odot) < 10$. These galaxies are the least massive ones in our sample and generally have blue, metal-poor GCs. *Middle*: coloured circles show GCs for host masses with $10 \le \log(M_{\mathrm{Host}}/M_\odot) < 11$. This bin contains the most GCs and those sample the full range of colours and metallicities. *Bottom*: highest mass bin with $\log(M_{\mathrm{Host}}/M_\odot) \ge 11$ containing GCs with a broad range of metallicities and colours, except for the most metal-poor ones. The grey dots and line give the full sample and the fit, respectively. The black dotted line shows the fit to the respective mass bin.

mean metallicity by ∼0.15 dex, on the order of the random uncertainties. This offset might reflect the generally younger ages of GCs in low-mass galaxies, but a larger sample would be required to test whether this offset is real.

The intermediate mass bin ($10 \le \log(M_*/M_\odot) < 11$) contains the largest number of GCs and samples the full range of metallicities and colours. The bent shape of the CZR is visible in this mass bin and does not differ significantly from the one using the full sample.

The highest mass bin ($\log(M_*/M_\odot) > 11$) contains the GCs of the central galaxy FCC 213 (NGC 1399), FCC 219 and FCC 167. In this mass range, also a broad range of metallicities and colours is found, but the bluest, most metal-poor GCs are lacking ($g−z < 0.9$ and [M/H] $< −2.0$ dex). Nonetheless, using only these GCs still results in a non-linear CZR that is very similar to that of the full sample.

Although the least massive galaxies in our sample would possible result in a linear CZR simply due to the lack of red,
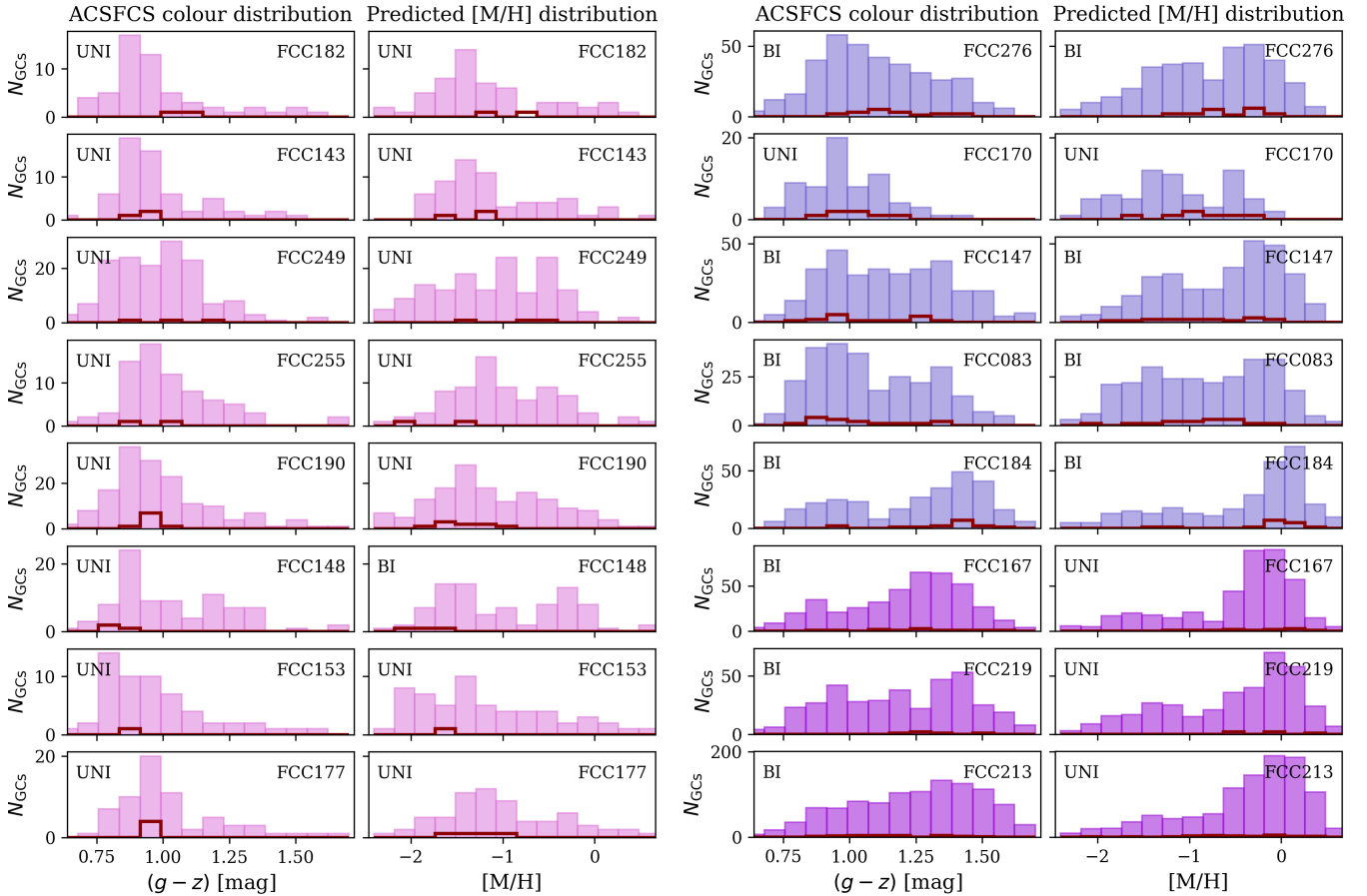
Fig. 9. Colour (*first* and *third panel*) and metallicity (*second* and *fourth panel*) distribution for 16 F3D galaxies that have a sufficient number of GC candidates in the ACSFCS catalogue from Jordán et al. (2015) to create a well sampled distribution. MDFs were inferred from the colour distributions using Eq. (3) with the best-fit parameters from our default CZR (Table A.2). The histograms are coloured based on the stellar mass of the host using three mass bins: $\log(M_{\rm Host}/M_\odot) < 10$ (pink), $10 \leq \log(M_{\rm Host}/M_\odot) < 11$ (blue), and $\log(M_{\rm Host}/M_\odot) \geq 11$ (purple). The red histograms show the GCs in our sample. In the top left corner of each panel, the distributions are classified as bimodal ("BI") or unimodal ("UNI") based on the GMM test described in the text.

metal-rich GCs, we cannot find indications of different CZR shapes as a function of stellar mass. GCs of the intermediate and high mass galaxies lie on the same track. Nonetheless, the deviations we found with some literature CZRs could lie in the different galaxy masses that are probed. M 87 studied by Villaume et al. (2019) is a giant ETG several times more massive than even FCC 213 (e.g. Wu & Tremaine 2006; Forte et al. 2012), so we cannot directly compare our GCs to those of M 87. Also the CZR of Usher et al. (2012) is based on five galaxies with $M_* > 10^{10.5}\,M_\odot$ (Forbes et al. 2017; Tamm et al. 2012). The CZR of Harris et al. (2017) is based on Centaurus A which has a stellar mass $M_* \sim 10^{11}\,M_\odot$ (Woodley 2006; Woodley et al. 2007, 2010b).

Alternatively, the different CZRs could reflect different environments. Many of the galaxies studied in the literature are the most massive galaxy of their group or cluster and thus might have unique assembly histories. In our sample, FCC 213 only constitutes a fraction of GCs and we could also include the GCs of low-mass galaxies with stellar masses $<10^{10}\,M_\odot$, a regime where the CZR of GCs is not yet explored. Using photometry of GCs in the core region of the Virgo in comparison to the MW, Powalka et al. (2016) found indications that the environment has an influence on colour–colour relations that in part are caused by chemical abundance variations. Therefore, they argue that relations derived in one environment might not be applicable

to other environments. The brightest GCs in our sample, however, appear to follow the same [Fe/H]−[M/H] relation as the stars in the MW, although a larger sample would be required to further determine the abundance pattern of GCs in relation to the environment.

5.3. Globular cluster metallicity distributions

The non-linear CZR of the F3D GCs has consequences for the MDFs of these galaxies. We can use our empirical relation to translate the extensive photometric GC catalogues from Jordán et al. (2015) to metallicity distributions and hence study the effect of this CZR in more detail. As examples, we picked 16 galaxies that were part of F3D and the ACSFCS to translate their ACSFCS GC colour distributions into metallicity distributions using Eq. (3) with the best-fitting parameters from our CZR. We selected all GC candidates with a probability of being a GC (pGC) greater than 50% (see Jordán et al. 2015 for details). This yields predictions for the metallicity distributions that would satisfy our CZR, shown in Fig. 9. The galaxies in this figure are ordered by increasing stellar mass. For comparison, we also show the confirmed GCs in our sample. We note again that our sample is deficient in the bluest GCs ($g - z < 0.8$ mag), possibly also because F3D covers the central parts of galaxies, while the relative number of blue GCs typically increases

with galactocentric radius (e.g. Faifer et al. 2011). Additionally, because the spatial coverage of the ACSFCS catalogue is limited, the ACSFCS colour distributions shown here might be deficient in blue GCs compared to the total GC distribution. However, these blue GCs are likely to be metal-poor and thus should not affect the bent shape of the CZR.

We quantified the shapes of the colour and metallicity distributions using the Gaussian mixture modelling (GMM) algorithm of Muratov & Gnedin (2010). This algorithm is a improved version of the KMM code (Ashman & Zepf 1992) and can be used to test whether a distribution is uni- or bimodal. GMM determines the best-fitting parameters of a unimodal and bimodal distribution and uses a bootstrap method to determine whether the bimodal solution is preferred. Following the suggestions of Muratov & Gnedin (2010), we consider a distribution to be bimodal if the distribution has a negative kurtosis, the relative distance between the two peaks is $D > 2$, and the bimodal solution is preferred with a probability $p > 0.9$. In Fig. 9, we noted the bimodal and unimodal distributions with "BI" and "UNI", respectively. In the GMM test, we assumed equal-width modes (homosedastic case) and this choice can influence the result (Beasley et al. 2018).

The GMM test shows that the lower mass galaxies tend to have unimodal colour distributions with a dominant peak at ~0.9 mag, while the high-mass galaxies have bimodal colour distributions. The relative number of red GCs increases with galaxy mass. The MDFs, however, show a more diverse behaviour because of the non-linear shape of our CZR that smears out blue peaks to broad metal-poor distributions. At low galaxy masses, our CZR at blue colours translates the blue, unimodal colour distributions to broader unimodal MDFs with a peak at low GC metallicities. At intermediate masses (e.g. FCC 276, FCC 147 and FCC 083, $\log(M_*/M_\odot) \sim 10.5$), bimodal colour distributions with roughly equal numbers of red and blue GCs lead to bimodal MDFs with a broader metal-poor peak. FCC 170 is an outlier in this, and despite its high stellar mass $\log(M_*/M_\odot) \sim 10.4$ (Iodice et al. 2019), shows a unimodal blue distribution with a relatively low number of GCs in total.

At the highest galaxy masses ($\log(M_*/M_\odot) > 11$, FCC 167, FCC 219, and FCC 213), the minor blue peak is smeared out to a tail of metal-poor GCs, resulting in unimodal MDFs with a dominant peak at high GC metallicities. This comparison shows that even with this non-linear CZR, not only unimodal MDFs are found. Instead, a diversity of MDFs is expected from our CZR and their modality appears to depend on the host galaxy.

5.4. Implications for galaxy assembly

Most galaxy formation theories explain GC colour and consequently metallicity bimodality by the existence of two distinct populations with different mean metallicities that are connected to different formation places. The bimodality has been linked to a two-stage formation scenario for massive galaxies (e.g. Ashman & Zepf 1992; Forbes et al. 1997; Côté et al. 1998; Beasley et al. 2002, 2018; Brodie & Strader 2006; Lee & Jang 2016) and is also expected in the hierarchical merger scheme of galaxy formation (e.g. Muratov & Gnedin 2010; Tonini 2013; Li & Gnedin 2014; Choksi et al. 2018; Kruijssen et al. 2019). It is assumed that the red, metal-rich GCs either form in situ in massive halos around the peak of star formation or during major mergers of gas-rich galaxies together with the bulk of in situ stars. They share the high metallicity of the stars because both are set by the local mass-metallicity relation (e.g. Shapiro et al. 2010). In contrast, the metal-poor GCs form in smaller haloes

from metal-poor gas and are accreted to the main galaxy in a series of hierarchical mergers (see also Forbes & Remus 2018).

As consequence of the steep slope of our CZR at blue colours, it predicts unimodal MDFs with a broad metal-poor component for galaxies with low mass and a low fraction of red GCs. In contrast, truly bimodal MDFs are expected for intermediate massive galaxies that have roughly a similar number of red and blue GCs, while at the highest galaxy masses, unimodal MDFs with a peak at high (~solar) metallicities are expected. In context of hierarchical assembly scenarios, this CZR still allows to conclude that the reddest GCs were formed in situ and the bluest, most metal-poor GCs were formed in metal-poor dwarfs. This conclusion is also supported, for example, by the often observed different radial profiles of both components (e.g. Harris 2009a,b; Faifer et al. 2011) and different kinematics (e.g. Schuberth et al. 2010; Strader et al. 2011; Pota et al. 2013). As we showed in the Paper I, especially red GCs trace the metallicity of the host galaxy, as would be expected from an in situ population, while the blue GCs show large metallicity differences.

However, for GCs of intermediate colours, their origin is less clear than a bimodal colour distribution would suggest because they fall in the region of the CZR that shows a steep slope and thus can have a large range of metallicities. This could indicate that those GCs are a mixed population of both in situ and ex-situ GCs. For example, they could consist of a population of more metal-poor GCs that has formed in situ very early-on from less enriched gas, or they are the relatively more metal-rich GCs accreted from more massive satellites. The unimodal MDFs of the most massive galaxies could then be an effect of a rich merger history during which the GCs of galaxies with different but mostly high masses were accreted, while the bimodal MDF of lower mass galaxies were created by a larger number of minor mergers (e.g. Xu et al. 2012; O'Leary et al. 2020). Nonetheless, the merger history of individual galaxies can be very diverse as cosmological simulations suggest and thus a model of the merger history would be required to interpret colour and metallicity distributions.

As an alternative to the two-phase scenarios, Yoon et al. (2006) showed that a strongly non-linear CZR can create a bimodal colour distribution from a unimodal MDF (see also Yoon et al. 2011a,b; Kim et al. 2013; Chung et al. 2016) without invoking the presence of two distinct populations. Instead, they proposed theoretical non-linear CZRs based on detailed stellar population modelling. Recently, Lee et al. (2019) modelled the colour distributions of a large number of galaxies in the Fornax and Virgo clusters and found that most of the GC system colour bimodality can be explained by unimodal MDFs and a non-linear CZR. They attribute the observed diversity in colour distributions to the mean metallicity of the GC system, where more massive galaxies have a more metal-rich GC system. Our non-linear CZR indeed finds unimodal, metal-poor MDFs for the least massive and unimodal, metal-rich MDFs for the most massive galaxies, in accordance to this picture. However, for intermediate mass galaxies, we still find bimodal MDFs and in the high mass galaxies, we still observe a tail of more metal-poor GCs. Although it is possible that this tail consists of only GCs that were formed in situ under different conditions, the bimodal MDFs in less massive galaxies rather supports the idea of distinct populations, although with less strict metallicity differences than the colour distributions might suggest. This in agreement with the results from recent hydrodynamical simulations that have shown that a one-to-one relation between metallicity and in situ or accreted population is not given (Forbes & Remus 2018).

6. Conclusions

We have studied the colour–metallicity relation (CZR) from a sample of 187 GCs of 23 galaxies in the Fornax cluster that were observed as part of the F3D project. These galaxies cover a range in stellar masses between 10^8 and 10^{11} $M_\odot$. Our main results are as follows:

– We derived metallicities with full spectral fitting and compared them to photometry mainly from the ACSFCS ($g - z$ colours, Jordán et al. 2015). The resulting CZR is non-linear. It is shallow at red colours and significantly steepens at bluer colours. The relation can be described by a quadratic function or a piecewise linear function with a breakpoint at $(g-z) \sim 1.1$ mag. A linear relation is not sufficient to describe the shape of the CZR.

– Although our default approach assumes a GC age ≥ 8 Gyr, we tested this assumption by also fitting the GC ages. This shows that the metallicities and the CZR are insensitive to the age prior, and the best-fitting ages are old (≥ 8 Gyr) with very few exceptions. We only found a weak age-metallicity relation that appears to be mostly driven by the mass of the host because the low mass galaxies in our sample tend to have younger, more metal-poor GCs.

– Using a small sub-sample of the very brightest GCs, we derived [α/Fe] abundances and found a negative correlation with metallicities. The more metal-poor GCs seem to be more α-enhanced.

– We derived the MZR and found a weak correlation between GC mass and metallicity, in agreement with previous studies. This finding motivates to also apply the CZR to fainter GCs missing from our sample due to sensitivity and S/N limitations. These fainter GCs should sample the same colour range, but might be slightly more metal-poor due to this MZR. It is unlikely that incompleteness affects the shape of the CZR.

– Our CZR generally agrees with literature CZRs at red colours and high metallicities, while there are larger deviations at bluer colours and lower metallicities. We discuss that this might be an effect of the different galaxy masses probed in different studies. Since our sample also includes usually unexplored low-mass galaxies, we were able to measure the metallicities of a large number of blue GCs. When we binned the sample by host mass, we found the same non-linear CZR even for the most massive galaxies.

– Applying the non-linear CZR to photometric GC colour distributions predicts a diversity of MDFs. The shape of the CZR implies that massive galaxies with relatively small blue GC populations have a unimodal MDF with a peak at high and a tail towards lower metallicities. Galaxies with equal numbers of red and blue GCs can truly have a bimodal metallicity distribution, while low mass galaxies show a unimodal MDF with a metal-poor peak, resulting from the lack of red GCs.

– In the context of galaxy assembly, the MDFs predicted by our CZR support different origins for GCs at the metal-poor and metal-rich end of the distribution. While the most-metal rich GCs are likely to have formed in situ in the host galaxy, the most metal-poor GCs were possibly accreted from low-mass dwarf galaxies. However, the shape of the CZR allows a variety of metallicities for GCs with intermediate colours and this could indicate a diverse origin for these GCs. They might be a mixture of more metal-poor GCs reflecting the metal-poor end of the in situ GC distribution and the relatively more metal-rich GCs accreted from more massive galaxies.

GCs are important tracers of galaxy assembly and to use them to their full capacity, constraining the CZR is a crucial step. In this work, we could derive a non-linear CZR in the Fornax cluster, using galaxies of a variety of different masses that challenges the simplistic division of GCs into in situ and accreted solely based on their colour. Although studies in different environments and including more low-mass host galaxies are still needed, the CZR shows that modelling individual merger histories is required to interpret colour and metallicity distributions.

References

Alves-Brito, A., Hau, G. K. T., Forbes, D. A., et al. 2011, MNRAS, 417, 1823
Ashman, K. M., & Zepf, S. E. 1992, ApJ, 384, 50
Astropy Collaboration (Robitaille, T. P., et al.) 2013, A&A, 558, A33
Astropy Collaboration (Price-Whelan, A. M., et al.) 2018, AJ, 156, 123
Bailin, J., & Harris, W. E. 2009, ApJ, 695, 1082
Barmby, P., Huchra, J. P., Brodie, J. P., et al. 2000, AJ, 119, 727
Beasley, M. A., Baugh, C. M., Forbes, D. A., Sharples, R. M., & Frenk, C. S. 2002, MNRAS, 333, 383
Beasley, M., Bridges, T., Peng, E., et al. 2008, MNRAS, 386, 1443
Beasley, M. A., Trujillo, I., Leaman, R., & Montes, M. 2018, Nature, 555, 483
Blakeslee, J. P., Jordán, A., Mei, S., et al. 2009, ApJ, 694, 556
Blakeslee, J. P., Cantiello, M., & Peng, E. W. 2010, ApJ, 710, 51
Blakeslee, J. P., Cho, H., Peng, E. W., et al. 2012, ApJ, 746, 88
Böcker, A., Leaman, R., van de Ven, G., et al. 2020, MNRAS, 491, 823
Boecker, A., Leaman, R., van de Ven, G., et al. 2019, MNRAS, 2678
Brodie, J. P., & Strader, J. 2006, ARA&A, 44, 193
Brodie, J. P., Strader, J., Denicoló, G., et al. 2005, AJ, 129, 2643
Brodie, J. P., Romanowsky, A. J., Strader, J., et al. 2014, ApJ, 796, 52
Caldwell, N., & Romanowsky, A. J. 2016, ApJ, 824, 42
Caldwell, N., Schiavon, R., Morrison, H., Rose, J. A., & Harding, P. 2011, AJ, 141, 61
Cantiello, M., & Blakeslee, J. P. 2007, ApJ, 669, 982
Cantiello, M., Blakeslee, J. P., Raimondo, G., et al. 2014, A&A, 564, L3
Cappellari, M. 2017, MNRAS, 466, 798
Cappellari, M., & Emsellem, E. 2004, PASP, 116, 138
Cenarro, A. J., Beasley, M. A., Strader, J., Brodie, J. P., & Forbes, D. A. 2007, AJ, 134, 391
Chandar, R., Puzia, T. H., Sarajedini, A., & Goudfrooij, P. 2006, ApJ, 646, L107
Chies-Santos, A. L., Larsen, S. S., Cantiello, M., et al. 2012, A&A, 539, A54
Cho, H., Blakeslee, J. P., Chies-Santos, A. L., et al. 2016, ApJ, 822, 95
Choksi, N., & Gnedin, O. Y. 2019, MNRAS, 488, 5409
Choksi, N., Gnedin, O. Y., & Li, H. 2018, MNRAS, 480, 2343
Chomiuk, L., Strader, J., & Brodie, J. P. 2008, AJ, 136, 234
Chung, C., Yoon, S.-J., Lee, S.-Y., & Lee, Y.-W. 2016, ApJ, 818, 201
Cohen, J. G., Blakeslee, J. P., & Ryzhov, A. 1998, ApJ, 496, 808
Cohen, J. G., Blakeslee, J. P., & Côté, P. 2003, ApJ, 592, 866
Côté, P., Marzke, R. O., & West, M. J. 1998, ApJ, 501, 554
Côté, P., Marzke, R. O., West, M. J., & Minniti, D. 2000, ApJ, 533, 869
El-Badry, K., Quataert, E., Weisz, D. R., Choksi, N., & Boylan-Kolchin, M. 2019, MNRAS, 482, 4528
Fahrion, K., Georgiev, I., Hilker, M., et al. 2019a, A&A, 625, A50
Fahrion, K., Lyubenova, M., van de Ven, G., et al. 2019b, A&A, 628, A92

Fahrion, K., Lyubenova, M., Hilker, M., et al. 2020, A&A, 637, A26
Faifer, F. R., Forte, J. C., Norris, M. A., et al. 2011, MNRAS, 416, 155
Falcón-Barroso, J., Sánchez-Blázquez, P., Vazdekis, A., et al. 2011, A&A, 532, A95
Ferguson, H. C. 1989, AJ, 98, 367
Forbes, D. A., & Remus, R.-S. 2018, MNRAS, 479, 4760
Forbes, D. A., Brodie, J. P., & Grillmair, C. J. 1997, AJ, 113, 1652
Forbes, D. A., Beasley, M. A., Brodie, J. P., & Kissler-Patig, M. 2001, ApJ, 563, L143
Forbes, D., Spitler, L., Strader, J., et al. 2011, MNRAS, 413, 2943
Forbes, D. A., Sinpetru, L., Savorgnan, G., et al. 2017, MNRAS, 464, 4611
Forte, J. C., Vega, E. I., & Faifer, F. 2012, MNRAS, 421, 635
Galleti, S., Bellazzini, M., Buzzoni, A., Federici, L., & Fusi Pecci, F. 2009, A&A, 508, 1285
Harris, W. E. 1996, AJ, 112, 1487
Harris, W. E. 2009a, ApJ, 699, 254
Harris, W. E. 2009b, ApJ, 703, 939
Harris, W. E. 2010, Philos. Trans. R. Soc. London Ser. A, 368, 889
Harris, W. E., & Canterna, R. 1979, ApJ, 231, L19
Harris, W. E., Whitmore, B. C., Karakla, D., et al. 2006, ApJ, 636, 90
Harris, W. E., Morningstar, W., Gnedin, O. Y., et al. 2014, ApJ, 797, 128
Harris, W. E., Blakeslee, J. P., Whitmore, B. C., et al. 2016, ApJ, 817, 58
Harris, W. E., Ciccone, S. M., Eadie, G. M., et al. 2017, ApJ, 835, 101
Hempel, M., Kissler-Patig, M., Puzia, T. H., & Hilker, M. 2007, A&A, 463, 493
Hilker, M., Infante, L., & Richtler, T. 1999, A&AS, 138, 55
Iodice, E., Sarzi, M., Bittner, A., et al. 2019, A&A, 627, A136
Jordán, A., Blakeslee, J. P., Côté, P., et al. 2007, ApJS, 169, 213
Jordán, A., Peng, E. W., Blakeslee, J. P., et al. 2015, ApJS, 221, 13
Kartha, S. S., Forbes, D. A., Alabi, A. B., et al. 2016, MNRAS, 458, 105
Katz, H., & Ricotti, M. 2014, MNRAS, 444, 2377
Kim, H.-S., Yoon, S.-J., Sohn, S. T., et al. 2013, ApJ, 763, 40
Kruijssen, J. M. D., Pfeffer, J. L., Crain, R. A., et al. 2019, MNRAS, 486, 3134
Kundu, A., & Whitmore, B. C. 2001, AJ, 121, 2950
Kuntschner, H., Ziegler, B. L., Sharples, R. M., Worthey, G., & Fricke, K. J. 2002, A&A, 395, 761
Larsen, S. S., Brodie, J. P., Huchra, J. P., Forbes, D. A., & Grillmair, C. J. 2001, AJ, 121, 2974
Leaman, R., Venn, K. A., Brooks, A. M., et al. 2013, ApJ, 767, 131
Lee, M. G., & Jang, I. S. 2016, ApJ, 822, 70
Lee, S.-Y., Chung, C., & Yoon, S.-J. 2019, ApJS, 240, 2
Li, H., & Gnedin, O. Y. 2014, ApJ, 796, 10
Liu, Y., Peng, E. W., Jordán, A., et al. 2019, ApJ, 875, 156
Madau, P., & Dickinson, M. 2014, ARA&A, 52, 415
Martín-Navarro, I., Vazdekis, A., Falcón-Barroso, J., et al. 2018, MNRAS, 475, 3700
Martocchia, S., Cabrera-Ziri, I., Lardo, C., et al. 2018, MNRAS, 473, 2688
Mieske, S., Hilker, M., Infante, L., & Jordán, A. 2006, AJ, 131, 2442
Muratov, A. L., & Gnedin, O. Y. 2010, ApJ, 718, 1266
Norris, M. A., Sharples, R. M., Bridges, T., et al. 2008, MNRAS, 385, 40
O'Leary, J. A., Moster, B. P., Naab, T., & Somerville, R. S. 2020, MNRAS, submitted [arXiv:2001.02687]
Peng, E. W., Ford, H. C., & Freeman, K. C. 2004, ApJ, 602, 705
Peng, E. W., Jordán, A., Côté, P., et al. 2006, ApJ, 639, 95
Pierce, M., Beasley, M. A., Forbes, D. A., et al. 2006a, MNRAS, 366, 1253

Pierce, M., Bridges, T., Forbes, D. A., et al. 2006b, MNRAS, 368, 325
Pietrinferni, A., Cassisi, S., Salaris, M., & Castelli, F. 2004, ApJ, 612, 168
Pietrinferni, A., Cassisi, S., Salaris, M., & Castelli, F. 2006, ApJ, 642, 797
Pinna, F., Falcón-Barroso, J., Martig, M., et al. 2019, A&A, 623, A19
Pota, V., Graham, A. W., Forbes, D. A., et al. 2013, MNRAS, 433, 235
Powalka, M., Puzia, T. H., Lançon, A., et al. 2016, ApJ, 829, L5
Puzia, T. H., Kissler-Patig, M., Thomas, D., et al. 2005, A&A, 439, 997
Puzia, T. H., Kissler-Patig, M., & Goudfrooij, P. 2006, ApJ, 648, 383
Reina-Campos, M., Kruijssen, J. M. D., Pfeffer, J. L., Bastian, N., & Crain, R. A. 2019, MNRAS, 486, 5838
Richtler, T. 2006, Bull. Astron. Soc. India, 34, 83
Sarzi, M., Iodice, E., Coccato, L., et al. 2018, A&A, 616, A121
Schuberth, Y., Richtler, T., Hilker, M., et al. 2010, A&A, 513, A52
Sesto, L. A., Faifer, F. R., Smith Castelli, A. V., Forte, J. C., & Escudero, C. G. 2018, MNRAS, 479, 478
Shapiro, K. L., Genzel, R., & Förster Schreiber, N. M. 2010, MNRAS, 403, L36
Sharina, M. E., Afanasiev, V. L., & Puzia, T. H. 2006, MNRAS, 372, 1259
Sinnott, B., Hou, A., Anderson, R., Harris, W. E., & Woodley, K. A. 2010, AJ, 140, 2101
Spitler, L. R., Larsen, S. S., Strader, J., et al. 2006, AJ, 132, 1593
Strader, J., & Smith, G. H. 2008, AJ, 136, 1828
Strader, J., Brodie, J. P., Cenarro, A. J., Beasley, M. A., & Forbes, D. A. 2005, AJ, 130, 1315
Strader, J., Brodie, J. P., Spitler, L., & Beasley, M. A. 2006, AJ, 132, 2333
Strader, J., Caldwell, N., & Seth, A. C. 2011, AJ, 142, 8
Tamm, A., Tempel, E., Tenjes, P., Tihhonova, O., & Tuvikene, T. 2012, A&A, 546, A4
Tonini, C. 2013, ApJ, 762, 39
Usher, C., Forbes, D. A., Brodie, J. P., et al. 2012, MNRAS, 426, 1475
Usher, C., Forbes, D. A., Brodie, J. P., et al. 2015, MNRAS, 446, 369
Usher, C., Pfeffer, J., Bastian, N., et al. 2018, MNRAS, 480, 3279
Usher, C., Brodie, J. P., Forbes, D. A., et al. 2019, MNRAS, 490, 491
Vazdekis, A., Casuso, E., Peletier, R. F., & Beckman, J. E. 1996, ApJS, 106, 307
Vazdekis, A., Sánchez-Blázquez, P., Falcón-Barroso, J., et al. 2010, MNRAS, 404, 1639
Vazdekis, A., Ricciardelli, E., Cenarro, A. J., et al. 2012, MNRAS, 424, 157
Vazdekis, A., Coelho, P., Cassisi, S., et al. 2015, MNRAS, 449, 1177
Vazdekis, A., Koleva, M., Ricciardelli, E., Röck, B., & Falcón-Barroso, J. 2016, MNRAS, 463, 3409
Villaume, A., Romanowsky, A. J., Brodie, J., & Strader, J. 2019, ApJ, 879, 45
Woodley, K. A. 2006, AJ, 132, 2424
Woodley, K. A., Harris, W. E., Beasley, M. A., et al. 2007, AJ, 134, 494
Woodley, K. A., Harris, W. E., Puzia, T. H., et al. 2010a, ApJ, 708, 1335
Woodley, K. A., Gómez, M., Harris, W. E., Geisler, D., & Harris, G. L. H. 2010b, AJ, 139, 1871
Worthey, G. 1994, ApJS, 95, 107
Wu, X., & Tremaine, S. 2006, ApJ, 643, 210
Xu, C. K., Zhao, Y., Scoville, N., et al. 2012, ApJ, 747, 85
Yoon, S.-J., Yi, S. K., & Lee, Y.-W. 2006, Science, 311, 1129
Yoon, S.-J., Lee, S.-Y., Blakeslee, J. P., et al. 2011a, ApJ, 743, 150
Yoon, S.-J., Sohn, S. T., Lee, S.-Y., et al. 2011b, ApJ, 743, 149
Zepf, S. E., & Ashman, K. M. 1993, MNRAS, 264, 611
Zhang, H.-X., Puzia, T. H., Peng, E. W., et al. 2018, ApJ, 858, 37
Zinn, R. 1985, ApJ, 293, 424

Appendix A: Different metallicity measurements

Table A.1. Overview of different approaches to determine metallicities from the GCs.

	Method name	Description
A	E-MILES	baseFe, age ≥ 8 Gyr
B	Scaled solar MILES	$[\alpha/\text{Fe}] = 0$ dex, age ≥ 8 Gyr
C	α-enhanced MILES	$[\alpha/\text{Fe}] = 0.4$ dex, age ≥ 8 Gyr
D	Full E-MILES	baseFe, no age constraint
E	Line-strength indices	age > 10 Gyr

Notes. Method A is the default approach, as also used in Paper I.

Our default approach to measure GC metallicities used the E-MILES SSP models with an age constraint ≥ 8 Gyr. In the following, we present the CZR using different approaches to fit metallicities based on a smaller sub-sample of 135 GCs with $S/N > 10 \, \text{Å}^{-1}$. Besides E-MILES models with and without age constraint, we also used the scaled solar MILES and the α-enhanced MILES models. They have smaller wavelength range and have $[\alpha/\text{Fe}] = 0$ dex (scaled solar) and 0.4 dex (α-enhanced) at all metallicities, respectively.

In addition to full spectral fitting, we also determined metallicities of 135 GCs with $S/N > 10 \, \text{Å}^{-1}$ from our sample using line-strength indices following the method described in Iodice et al. (2019) and Sarzi et al. (2018). To avoid contamination from sky residuals, a restricted wavelength region between 4800 and 5500 Å was used. The line-strengths of Hβ, Fe5015, Mg b, Fe5720, and Fe5335 were determined in the LIS system (Vazdekis et al. 2010, 2015) and were compared to the predictions from the MILES models (Vazdekis et al. 2012). The best-fitting values were determined using a Markov-chain-Monte-Carlo algorithm (Martín-Navarro et al. 2018).

Table A.1 lists the different approaches and we show the resulting CZRs in Fig. A.1 for both total and iron metallicities using $[\text{M/H}] = [\text{Fe/H}] + 0.75 \, [\alpha/\text{Fe}]$ as a conversion for the MILES models and the line-strength metallicities and the conversion derived in Sect. 4.3 for the E-MILES models. The default values derived with the E-MILES models (method A) are shown as the grey dots. In each case, we fitted the relation both with a quadratic equation (Eq. (2)) and a piecewise linear curve (Eq. (3)). The best-fitting parameters from least-square fits to the respective CZRs are reported in Table A.2.

Irrespectively of the chosen SSP models, we always found a steep slope of the colour–metallicity relation at low metallicities when using full spectral fitting with PPXF. Using line-strength indices (method E) to measure metallicities results in a significantly larger scatter and larger errorbars, possibly due to the limited wavelength range that is used, but we observed the same non-linear trend in the CZR.
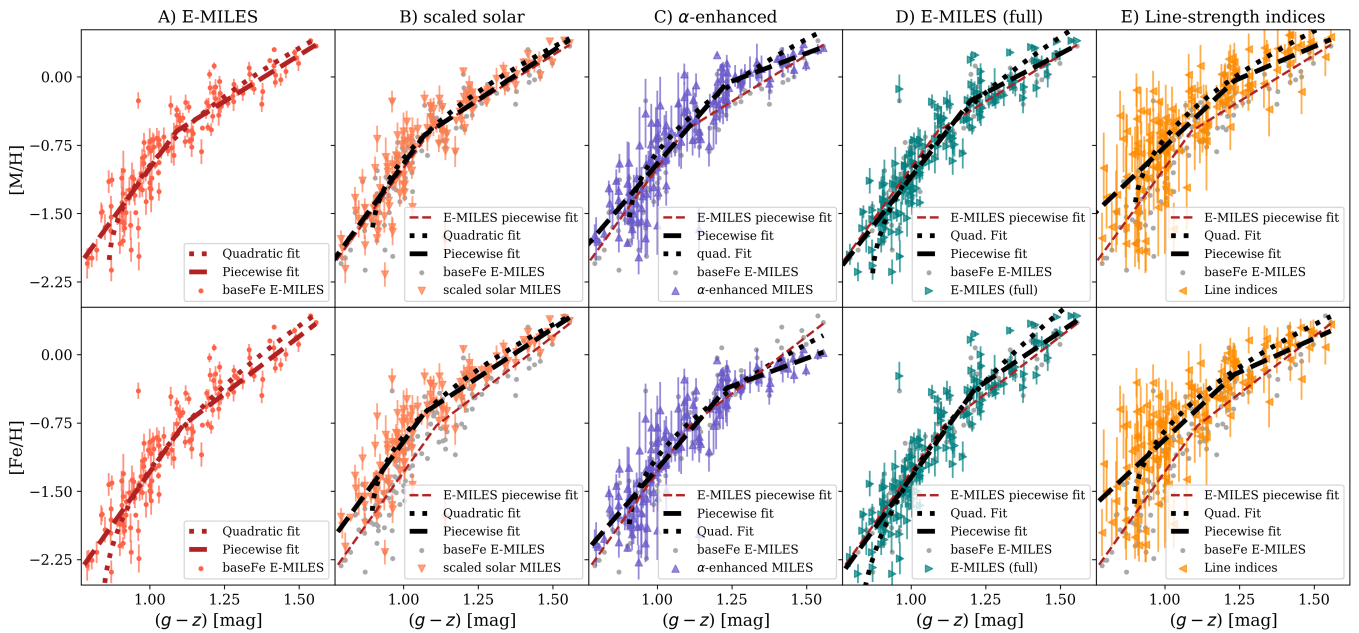
Fig. A.1. CZR for different metallicity measurement approaches (listed in Table A.1) based on total metallicities (*top*) and iron metallicities (*bottom*). *From left to right*: CZR using the E-MILES library with age constraint ≥ 8 Gyr (method A), scaled-solar MILES models (method B), α-enhanced MILES models (method C), E-MILES models without age constraint (method D), and line-strength indices (method E). The grey symbols show the points from method A as reference, and the lines show the respective fits. The best-fitting parameters are found in Table A.2.

Table A.2. Colour metallicity relation fit parameters when using total metallicities [M/H] or iron metallicities [Fe/H].

Method	a	b	c	m_1	b_1	m_2	b_2	x_0
[M/H]								
(A)	1.34 ± 0.01	0.46 ± 0.02	0.11 ± 0.01	4.51 ± 0.32	-5.51 ± 0.36	2.03 ± 0.20	-2.81 ± 0.36	1.09 ± 0.03
(B)	1.33 ± 0.01	0.49 ± 0.03	0.14 ± 0.01	4.51 ± 0.49	-5.47 ± 0.54	2.15 ± 0.26	-2.94 ± 0.54	1.07 ± 0.04
(C)	1.32 ± 0.01	0.48 ± 0.03	0.13 ± 0.01	4.58 ± 0.49	-5.53 ± 0.55	2.16 ± 0.26	-2.94 ± 0.54	1.07 ± 0.04
(D)	1.31 ± 0.01	0.39 ± 0.02	0.08 ± 0.01	4.21 ± 0.27	-5.31 ± 0.35	1.72 ± 0.39	-2.32 ± 0.35	1.20 ± 0.04
(E)	1.24 ± 0.01	0.45 ± 0.03	0.15 ± 0.02	3.11 ± 0.29	-3.88 ± 0.45	1.41 ± 0.71	-1.77 ± 0.44	1.23 ± 0.08
[Fe/H]								
(A)	1.37 ± 0.01	0.38 ± 0.02	0.07 ± 0.01	4.63 ± 0.31	-5.90 ± 0.38	2.51 ± 0.24	-3.55 ± 0.37	1.11 ± 0.03
(B)	1.33 ± 0.01	0.49 ± 0.03	0.14 ± 0.01	4.51 ± 0.49	-5.47 ± 0.54	2.15 ± 0.26	-2.94 ± 0.54	1.07 ± 0.04
(C)	1.47 ± 0.02	0.55 ± 0.03	0.13 ± 0.01	3.69 ± 0.26	-5.00 ± 0.36	1.64 ± 0.47	-2.51 ± 0.35	1.21 ± 0.05
(D)	1.34 ± 0.01	0.32 ± 0.02	0.05 ± 0.01	4.55 ± 0.27	-5.90 ± 0.38	2.21 ± 0.47	-3.06 ± 0.37	1.21 ± 0.04
(E)	1.32 ± 0.01	0.51 ± 0.03	0.15 ± 0.02	3.07 ± 0.29	-4.00 ± 0.46	1.48 ± 0.71	-2.04 ± 0.45	1.23 ± 0.09

Notes. The parameters a, b, and c refer to least-square fits with a quadratic equation (Eq. (2)), the m_1, b_1, m_2, b_2, and x_0 to the piecewise linear fit (Eq. (3)). The different methods are described in Table A.1.